A Novel Modeling and Design Method of Ferrite Pads to Enhance Comprehensive Performance in 11.1 kW Inductive Power Transfer System

Xian Zhang, Jie Liu, Runtian Dou, Liyuan Zhao, Zhicheng Xu, Jinghui Song, and Shenghu Liu

***Abstract*—Magnetic core parameters critically determine the transmission efficiency, power density, and overall performance of inductive power transfer systems. Conventional pad design methods predominantly rely on global optimization using simulation tools, often lacking clear physical interpretation. This study identifies a performance threshold for magnetic pads, beyond which further improvements in pad performance yield no meaningful gains in transmission efficiency. To quantify this threshold, an analytical model based on the boundary distribution of magnetic vector potential is developed, replacing conventional source-driven field approximations. The proposed formulation characterizes the internal magnetic field distribution and enables accurate determination of the threshold for magnetic pad sizing. Based on this insight, a sizing strategy is introduced to significantly enhance power density while maintaining high transmission efficiency. The method is validated through coupled electromagnetic–thermal simulations and experimental tests across a power range of 3–11.1 kW. Results show that, compared with an oversized reference pad—with a 25% increase in side length and a 56.2% increase in area—achieving only a 0.6% improvement in ac–ac transmission efficiency, the optimally sized pad improves efficiency by 3% over a downsized pad, which has a 25% reduction in side length and a 43.8% decrease in area, while also reducing peak temperature by 10 °C. These findings validate the proposed method's effectiveness in improving system power density and optimizing magnetic–thermal performance without compromising transmission efficiency.**

***Index Terms*—Analytical model, inductive power transfer (IPT), magnetic core, magnetic-thermal coupling.**

Received 22 May 2025; revised 29 July 2025 and 27 August 2025; accepted 27 September 2025. Date of publication 3 October 2025; date of current version 23 December 2025. This work was supported in part by the National Natural Science Foundation of China under Grant 52477005 and Grant 52122701, in part by the National Natural Science Foundation of Tianjin under Grant 22JCZDJC00620, in part by the Central Government Guides Local Science and Technology Development Foundation under Grant 236Z5201G, and in part by the S&T Program of Hebei under Grant 24464401D. Recommended for publication by Associate Editor M. Ponce-Silva. *(Corresponding author: Xian Zhang.)*

Xian Zhang, Jie Liu, Liyuan Zhao, Zhicheng Xu, Jinghui Song, and Shenghu Liu are with the State Key Laboratory of Smart Power Distribution Equipment and System, Hebei University of Technology, Tianjin 300132, ChinaHebei Key Laboratory of Equipment and Technology Demonstration of Flexible DC Transmission, Hebei University of Technology, Tianjin 300401, China (e-mail: zhangxian@hebut.edu.cn; 202331402005@stu.hebut.edu.cn; yuanerzhao@hebut.edu.cn; xzc@hebut.edu.cn; 202321401064@stu.hebut.edu.cn; 202431402121@stu.hebut.edu.cn).

Runtian Dou is with the School of Intelligent Manufacturing, Nanyang Institute of Technology, Nanyang 473004, China (e-mail: 202011401010@stu.hebut.edu.cn).

Color versions of one or more figures in this article are available at https://doi.org/10.1109/TPEL.2025.3617344.

Digital Object Identifier 10.1109/TPEL.2025.3617344

I. Introduction

INDUCTIVE power transfer (IPT) technology uses an alternating magnetic field as the transmission medium, enabling wireless power transfer between the transmitter and receiver of the system. In contrast to traditional wired transmission, IPT technology eliminates the need for physical electrical connections, thus reducing reliance on components such as cables and connectors, which enhances the overall safety of the power transfer system [1], [2]. In recent years, with the rise of high-power density electrical equipment, there has been growing interest in the application of IPT technology under high-power conditions. Due to advancements in fast-charging technology, the power rating of IPT systems has now reached several tens of kilowatts. This development holds significant potential for applications in electric vehicles, smart grids, underwater vehicles, and intelligent robotics [3], [4], [5].

In IPT systems, magnetic cores are typically added to the backside of the transmitting and receiving coils to regulate the spatial distribution of the coupling magnetic field and enhance the mutual inductance between the coils [6]. However, loosely coupled systems lead to higher magnetic flux leakage, especially under high-power conditions, where IPT systems also face challenges such as high losses and thermal runaway [7], [8], [9]. A conventional solution involves optimizing the magnetic core and coil structures to improve the magnetic field distribution in IPT systems, thereby enhancing power transfer efficiency, magnetic-thermal balance, and stray field safety performance [10], [11], [12]. In fact, the effect of the magnetic core on the system is generated by the superposition of the additional magnetic field induced by magnetization and the magnetic field generated by the current-carrying coils. This additional magnetic field is directly related to the size parameters of the magnetic core and its electromagnetic properties (permeability, conductivity). Given the selected materials, the electromagnetic parameters of the magnetic core are typically difficult to modify, making the design of appropriate size parameters key to ensuring the overall performance of the system. When the magnetic core is too small, magnetic leakage increases, transmission efficiency decreases, and thermal management challenges arise. On the other hand, if the magnetic core is too large, the system's power density decreases and structural flexibility is compromised. Therefore, analyzing the magnetic field distribution within the magnetic core based on Maxwell's theory and revealing the relationship

between the field distribution and the comprehensive performance of the IPT system is essential. This analysis provides a foundation for designing the magnetic core's optimal size parameters, contributing to further performance enhancement of the system.

In recent years, significant research has focused on the analysis of the spatial magnetic field distribution in IPT systems. The self-inductance and mutual inductance of coils integrated with magnetic cores under misalignment conditions are analyzed in [13]. The study also investigates the influence of parameters such as the number of coil turns and current frequency on the mutual inductance. In [14], the spatial magnetic field distribution of the system under the influence of magnetic cores is analytically derived using the Fourier-Bessel transform and the double Fourier transform method. This work initiates the application of classical Maxwell theory-based analytical approaches in IPT systems, as further developed in [15]. A method is proposed for analyzing the mutual inductance of rectangular coils at arbitrary positions, which further enhanced the degree of freedom in spatial magnetic field analysis for IPT systems in [16]. Although existing methods can accurately analyze the self-inductance and mutual inductance of coils under the influence of magnetic cores, theoretical research on the magnetic field distribution characteristics within the magnetic core remains limited. In addition, coil inductance only reflects the macroscopic manifestation of the magnetic field, and typically cannot intuitively reveal the distribution characteristics of the system's coupling magnetic field [17], [18]. Currently, the analysis of the magnetic field in IPT systems is primarily focused on the spatial region, and the magnetic field distribution within the core has yet to be fully explored. Establishing the analytical relationship between the magnetic field distribution within the core and its size parameters will provide more effective guidance for the design of magnetic core structures, ultimately improving the system's power density and overall performance [19], [20].

In this article, a novel theoretical modeling method is proposed for the magnetic pad in IPT systems to achieve optimal utilization of the magnetic core's capabilities. Based on the proposed model, an optimized design is implemented for ferrite core sizes and is successfully applied to an 11.1-kW-level IPT prototype operating across a broad power range.

Key contributions of this study include the following.

1) An interesting performance saturation phenomenon has been identified in the IPT magnetic pad, revealing a critical threshold beyond which further improvement in pad characteristics yields negligible gains in system-level efficiency. To investigate this behavior, an analytical method is proposed that replaces the complex source distribution with equivalent boundary magnetic vector potentials, enabling the derivation of the internal magnetic field distribution within the pad.
2) A design methodology for determining the sizes of magnetic pads is proposed, aiming to optimize the utilization of ferrite core performance in IPT systems, based on the identified saturation characteristics of the pad.
3) An 11.1-kW IPT prototype is fabricated to validate the effectiveness of the magnetic pad sizing method. Compared to the reference configuration, the optimally designed pad, based on the proposed method, achieves higher power density and improved magnetic-thermal balance, while maintaining the desired transmission efficiency.

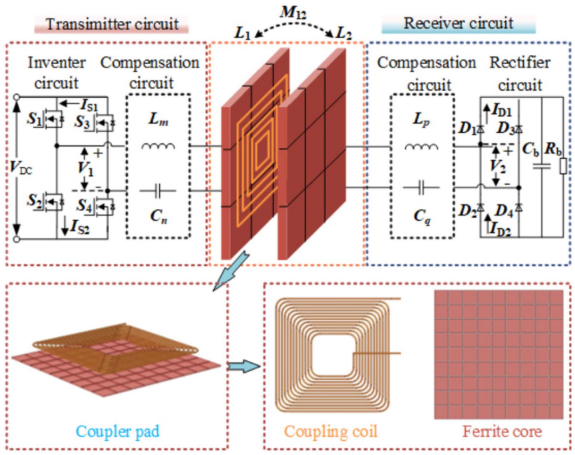

Fig. 1. Schematic of the IPT system with ferrite pads. M_{12}: Mutual inductance between the coupling coil. L_1 and L_2: Self-inductance of the transmitter and receiver.

II. Quasi-Static Field Modeling and Magnetic Core Design for IPT Coupling Mechanisms

A. Analysis of the Magnetic Energy Coupling Structure Model

A simplified diagram of the IPT system is illustrated in Fig. 1. The system consists of a power supply, inverter-rectifier stage, compensation network, magnetic coupling structure, and load. Among these, the magnetic coupling structure serves as the core component of IPT system, as it enhances magnetic coupling and mitigates magnetic flux leakage. To analyze the power transfer characteristics, the mutual inductance-based equivalent circuit model is typically employed for efficient characterization of both input and output behaviors. For any compensated IPT topology, the power transfer efficiency is inherently governed by the mutual inductance parameters of the system, which can be derived as follows:

$$M = \frac{\iint_D \boldsymbol{B} \cdot d\boldsymbol{S}}{I} \tag{1}$$

where D denotes the oriented surface bounded by the receiving coil, and $\boldsymbol{B}$ represents the magnetic flux density distributed over surface D within the magnetic coupling structure. This magnetic field is formed by the superposition of the excitation field generated by the energized coil L_1 and the induced fields from the magnetic cores on both sides. The transmission path and spatial distribution of the magnetic field critically influence the overall efficiency and operational safety of the system. On this basis, establishing an accurate magnetic field model of the IPT system provides a scientific foundation for magnetic design and serves as a valuable reference for system optimization.

B. Quasi-Static Field Modeling of the Coupling Region

The IPT system typically operates at frequencies below 100 kHz. When the angular frequency ω, relative permittivity ε, and electrical conductivity γ of the magnetic coupling structure

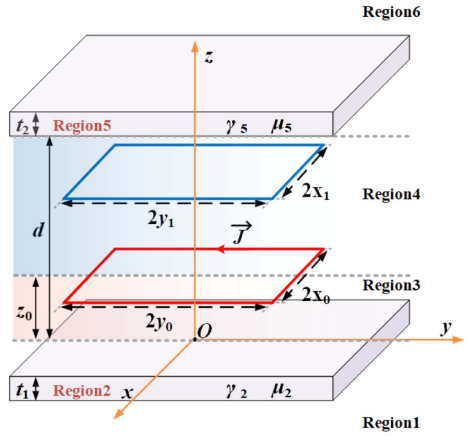

Fig. 2. Simplified model of the magnetic coupling structure in an IPT system.

satisfy the condition given in the following equation:

$$\omega\varepsilon \ll \gamma. \tag{2}$$

The displacement current within the magnetic core can be neglected. In addition, the coils are generally wound using litz wire, which significantly reduces the skin effect in conductors. Consequently, the system can be regarded as operating within a quasi-static magnetic field regime.

To simplify the modeling analysis, a single-turn conductor is considered as an example. Fig. 2 illustrates the magnetic coupling structure of the IPT system. The entire model is divided into six regions. Regions 2 and 5 correspond to magnetic core regions with infinite width. The parameters μ_2, μ_5, γ_2, and γ_5 represent the relative permeability and electrical conductivity of the cores. The core thicknesses on the transmitting and receiving sides are denoted as $t_1 = t_2 = t$. Regions 3 and 4 define the coupling area, where x_0, y_0 and x_1, y_1 represent the half-length and half-width dimensions of the transmitting and receiving coils, respectively. Regions 1 and 6 represent nonfunctional area.

Based on Maxwell's differential identity transformations, the governing magnetic field equation for the coupling region can be derived as follows:

$$\nabla^2 \boldsymbol{B} = j\omega\mu_r\mu_0\gamma\boldsymbol{B} \tag{3}$$

where j is the imaginary unit.

The magnetic flux density $\boldsymbol{B}$ in the coupling region can be calculated as the superposition of $\boldsymbol{B_t}$, generated by the transmitting coil, and $\boldsymbol{B_i}$, representing the equivalent induced field from the magnetic core. Since the excitation current of the planar coil is confined to the xy-plane, the use of the magnetic vector potential method for computing $\boldsymbol{B_t}$ simplifies the analysis. Given that the conductor's cross-sectional area is negligible compared to the overall dimensions of the magnetic coupling structure, the current distribution in the wire can be approximated as a line current, and the elemental current segment is represented as Idl. The magnetic vector potential $\boldsymbol{A_t}$, induced by the current source located at (x', y', z'), can be computed using the line integral expression

$$\boldsymbol{A_t}(x,y,z) = \frac{\mu_0}{4\pi}\oint_l \frac{I\boldsymbol{dl'}}{\sqrt{(x-x')^2+(y-y')^2+(z-z_0)^2}}. \tag{4}$$

For IPT systems employing rectangular coils, the magnetic vector potential in the coupling region can be computed using the double Fourier transform and its corresponding inverse transform, as described in [14]. The formulation is expressed as follows:

$$F(\omega_1,\omega_2,z) = \int_{-\infty}^{+\infty}\int_{-\infty}^{+\infty} f(x,y,z)\, e^{-j(x\omega_1+y\omega_2)}dxdy \tag{5}$$

$$f(x,y,z) = \frac{1}{4\pi^2}\int_{-\infty}^{+\infty}\int_{-\infty}^{+\infty} F(\omega_1,\omega_2,z)\, e^{j(x\omega_1+y\omega_2)}d\omega_1 d\omega_2. \tag{6}$$

By applying a double Fourier transform to both sides of (4), the frequency-domain expression of the magnetic vector potential $\boldsymbol{a_t}$ is obtained as follows:

$$\boldsymbol{a_t}(\omega_1,\omega_2,z) = \frac{\mu_0 I}{2}\frac{e^{-|z-z_0|\sqrt{{\omega_1}^2+{\omega_2}^2}}}{\sqrt{{\omega_1}^2+{\omega_2}^2}}\oint_l e^{-j(x'\omega_1+y'\omega_2)}\boldsymbol{dl'}. \tag{7}$$

Since the current in the planar coil has no component in the z-direction, the z-direction of the magnetic vector potential is zero. Its frequency-domain components can be computed as follows:

$$a_{t\omega_i} = \frac{(-1)^{i+1}j2\mu_0 I\sin(x_0\omega_1)\sin(y_0\omega_2)}{\omega_i\sqrt{{\omega_1}^2+{\omega_2}^2}}e^{-|z-z_0|\sqrt{{\omega_1}^2+{\omega_2}^2}} \tag{8}$$

where $i = 1, 2$.

By taking the curl of the frequency-domain magnetic vector potential $\boldsymbol{a_t}$, the components of the frequency-domain magnetic flux density $\boldsymbol{b_t}$ can be obtained as follows:

$$\begin{aligned} b_{t\omega_1} &= -\frac{\partial a_{t\omega_2}}{\partial z} \\ b_{t\omega_2} &= \frac{\partial a_{t\omega_1}}{\partial z} \\ b_{tz} &= j\omega a_{t\omega_2} - j\omega a_{t\omega_1}. \end{aligned} \tag{9}$$

Regions 1, 3, 4, and 6 are all air domains. The equivalent external magnetic field $\boldsymbol{B_i}$ induced by the magnetic core satisfies the following conditions:

$$\begin{aligned} \nabla \bullet \boldsymbol{B_i} &= 0 \\ \nabla \times \boldsymbol{B_i} &= 0. \end{aligned} \tag{10}$$

Applying the Fourier transform to the above differential equations yields the following relationships for the frequency-domain components of the induced magnetic field

$$j\omega_1 b_{i\omega 1} + j\omega_2 b_{i\omega 2} + \frac{\partial b_{iz}}{\partial z} = 0 \tag{11}$$

$$\omega_1 b_{i\omega 2} = \omega_2 b_{i\omega 1} \tag{12}$$

$$j\omega_2 b_{iz} = \frac{\partial b_{i\omega 2}}{\partial z}. \tag{13}$$

By combining (3), (11), (12), and (13), the control equation for the induced magnetic field $\boldsymbol{b_i}$ is obtained as follows:

$$\begin{aligned} \frac{\partial^2 \boldsymbol{b_i}}{\partial z^2} &= \left(\omega_1^2+\omega_2^2\right)\boldsymbol{b_i} \\ b_{i\omega 1} &= \frac{j\omega_1}{{\omega_1}^2+{\omega_2}^2}\frac{\partial b_{iz}}{\partial z}. \end{aligned} \tag{14}$$

The general solution for b_{iz} is as follows:

$$b_{iz} = C_{iz}e^{\sqrt{\omega_1^2+\omega_2^2}z} + C'_{iz}e^{-\sqrt{\omega_1^2+\omega_2^2}z}. \tag{15}$$

The solutions for C_{iz} and $C^{'}{}_{iz}$ need to be determined using the magnetic field boundary conditions at the interfaces. For mutual inductance calculation, it is sufficient to consider the superposition of $\boldsymbol{b_t}$ and $\boldsymbol{b_i}$. By combining (8) and (9), the z-component of $\boldsymbol{b_t}$ can be derived as follows:

$$\begin{aligned} b_{tz} &= \frac{2\mu_0 I\sqrt{{\omega_1}^2+\omega_2^2}\sin(x_0\omega_1)\sin(y_0\omega_2)}{\omega_1\omega_2} \\ &\quad\times e^{-(z-z_0)\sqrt{{\omega_1}^2+\omega_2^2}} \\ &= C_{tz}e^{-z\sqrt{{\omega_1}^2+\omega_2^2}}. \end{aligned} \tag{16}$$

The undetermined coefficients corresponding to the z-component of the induced magnetic field $\boldsymbol{b_i}$ are given as follows:

$$\begin{aligned} C_{iz} &= \frac{C_{tz}\left(P+e^{-2s_1\sqrt{{\omega_1}^2+\omega_2^2}}\right)}{PQ-1} \\ C'_{iz} &= \frac{C_{tz}e^{-2s_1\sqrt{{\omega_1}^2+\omega_2^2}}+C_{iz}}{P} \end{aligned} \tag{17}$$

where P and Q are intermediate variables, and the results are given as follows:

$$\begin{aligned} P &= \frac{2}{1-\frac{1}{\mu_2}+\left(1+\frac{1}{\mu_2}\right)\frac{m_2-1}{m_2+1}e^{-2\lambda_2 t}} \\ &\quad+\frac{2}{\left(1-\frac{1}{\mu_2}\right)\frac{m_2-1}{m_2+1}e^{2\lambda_2 t}+1+\frac{1}{\mu_2}}-1 \\ Q &= \frac{2e^{2\sqrt{\omega_1^2+\omega_2^2}d}}{(1+m_5)(1-e^{2\lambda_5 t})}+\frac{2e^{2\sqrt{\omega_1^2+\omega_2^2}d+2\lambda_5 t}}{(1-m_5)(1-e^{2\lambda_5 t})} \\ &\quad-e^{2\sqrt{\omega_1^2+\omega_2^2}d} \\ \lambda_i &= \sqrt{j\omega\mu_i\mu_0\gamma+\omega_1^2+\omega_2^2} \\ m_i &= \frac{\lambda_i}{\mu_i\sqrt{\omega_1^2+\omega_2^2}}. \end{aligned}$$

By applying the two-dimensional inverse Fourier transform, the z-component of the coupling magnetic field B_z can be obtained as follows:

$$B_z = \frac{1}{4\pi^2}\int_{-\infty}^{\infty}\int_{-\infty}^{\infty}(b_{tz}+b_{iz})\cdot e^{j(x\omega_1+y\omega_2)}d\omega_1 d\omega_2. \tag{18}$$

The magnetic flux Ψ linked with the loop can be calculated as follows:

$$\Psi = \iint_D \boldsymbol{B}\cdot d\boldsymbol{S} = \iint_D B_z dS. \tag{19}$$

For a multiturn coil system, the inductance can be calculated as follows:

$$L = \frac{\sum_{i=1}^{n}\left(\iint_{D_j}\sum_{j=1}^{n}B_{jz}dS\right)}{I} \tag{20}$$

$$M = \frac{\sum_{i=1}^{n}\left(\iint_{D_j}\sum_{j=1}^{n}B_{jz}dS\right)}{I} \tag{21}$$

TABLE I
DESIGN PARAMETERS OF THE COIL

Parameters	Value
Outer Side Length of the Transmitter Coil (mm)	380
Inner Side Length of the Transmitter Coil (mm)	144
Outer Side Length of the Receiver Coil (mm)	380
Inner Side Length of the Receiver Coil (mm)	144
Number of Turns	13
Distance between Pad and Coil (mm)	5
Distance between Two Coils (mm)	160

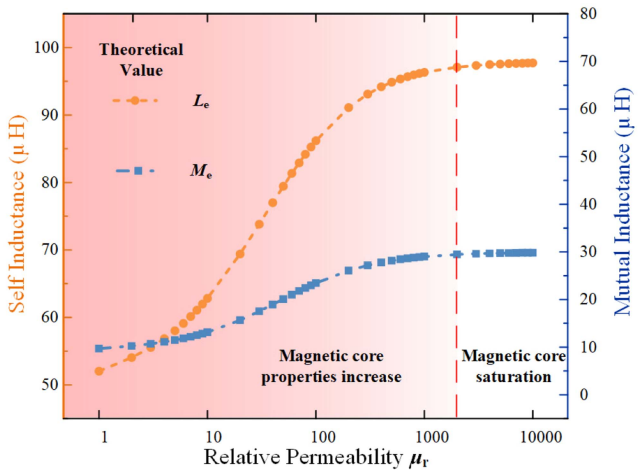

Fig. 3. Theoretical inductance values of the coils in the magnetic coupling structure.

where n denotes the number of turns in the coil, D_j represents the planar area enclosed by the jth turn, and B_{jz} is the z-component of the magnetic field jointly generated by the jth coil turn and the magnetic core.

Based on the theoretical model described above, the relationship between the coil's mutual and self-inductance and the magnetic permeability of the core can be analyzed. The magnetic coupling structure of the IPT system is simplified as a symmetric multiturn square coil configuration, with the magnetic core modeled as an isotropic, linear, and homogeneous material. The specific structural parameters of the coil and magnetic medium are listed in Table I.

Fig. 3 presents the theoretical values of self-inductance L_e and mutual inductance M_e of the IPT system's coupling structure, with the relative permeability μ_r chosen as the independent variable. The horizontal axis represents μ_r ranging from 1 to 10 000. As shown, both L_e and M_e exhibit an increasing trend with rising permeability; however, the rate of increase varies across different permeability intervals. In the range of $\mu_r = 1$ to 2000, both inductance parameters increase rapidly, indicating high sensitivity of the system's electrical characteristics to the core permeability. Specifically, L_e and M_e increase by 86.2% and 203.9%, respectively. As μ_r continues to rise, the sensitivity gradually decreases, and when μ_r increases from 2000 to 10 000, the growth curves for both parameters flatten, with respective increases of only 0.65% and 1.26% . This phenomenon can be attributed to the saturation of the core's magnetic response: as the relative

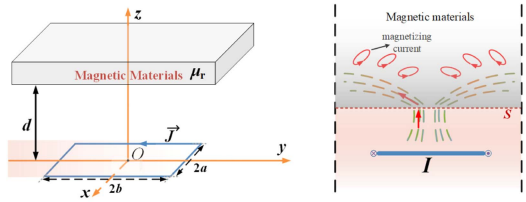

Fig. 4. (a) Equivalent model of magnetic core and coil. (b) Magnetic field lines and magnetization current distribution.

permeability reaches a sufficiently high level, the enhancement of the magnetic field induced by core magnetization approaches its theoretical limit, thereby reducing its additional contribution to coupling between the transmitting and receiving cores.

C. Internal Magnetic Field Distribution and Core Size Design

The above-mentioned analysis leads to the conclusion that the performance of the magnetic core approaches a saturation point once its parameters reach a certain range. This implies that beyond this threshold, the transmission performance of the IPT system cannot be further improved significantly. The dimensional parameters of the magnetic core are closely related to the power density, efficiency, and thermal characteristics of the IPT system. If the magnetic field distribution within the core can be accurately determined, the dimensional range corresponding to the performance saturation of the core can be identified. However, due to the presence of equivalent magnetization current sources and eddy current sources within the core, the internal magnetic field no longer satisfies the conditions described by (10). Consequently, solving for the magnetic field inside the core using a double Fourier transform becomes highly complex and computationally intensive. To address this challenge, this article proposes an analytical method that replaces the complex internal field sources with boundary magnetic vector potentials, thereby enabling efficient estimation of the internal magnetic field distribution.

In typical configurations, IPT coils are attached to the magnetic core on the same side and are positioned at a greater distance from the opposite-side core. As a result, the magnetic field distribution within the core is primarily influenced by the coil on the same side. The magnetic field distribution in the core can be analyzed using the simplified model shown in Fig. 4(a). When a current I is applied to the coil, in addition to the conduction current along the wire, macroscopic equivalent magnetization current sources are generated within the magnetic core. These magnetization currents exhibit complex spatial distributions, leading to distortion in the magnetic fields across both the coupling and core regions. The resulting magnetic flux lines and magnetization current distribution are illustrated in Fig. 4(b).

Fig. 5(a) illustrates the two-dimensional schematic of a simplified coupling structure model, where the gray rectangular region denotes the magnetic core domain to be analyzed. According to Helmholtz's theorem, when the magnetic vector potential distributions on the boundary interfaces S_{a+} and S_{b+} are identical, the magnetic field distributions within the magnetic

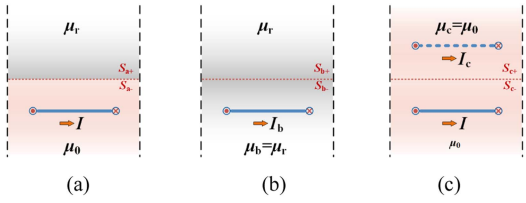

Fig. 5. Schematic diagram of magnetic core coupling mechanism model.

cores in Fig. 5(a) and (b) are equivalent. As indicated by (4), the magnetic vector potential $\boldsymbol{A}_{a+}$ on S_{a+} is jointly determined by the distribution of the current source I and the magnetic permeability μ_0. If a new set of electromagnetic parameters, I_b and μ_b, can be found such that $\boldsymbol{A}_{b\pm} = \boldsymbol{A}_{a+}$, then the solution obtained from the computational domain in Fig. 5(b) can be employed as a substitute for that in Fig. 5(a).

Without loss of generality, let $\mu_b = \mu_r$, thereby transforming the problem into solving the magnetic field distribution of a rectangular coil in a homogeneous medium. The magnetic vector potential on the boundary interface S_b can then be computed as follows:

$$A_{bx\pm} = \frac{\mu_0 \mu_r I_b}{4\pi} \ln\left[\frac{(-a-x+r_2)(a-x+r_4)}{(a-x+r_1)(-a-x+r_3)}\right]$$
$$A_{by\pm} = \frac{\mu_0 \mu_r I_b}{4\pi} \ln\left[\frac{(b-y+r_1)(-b-y+r_3)}{(-b-y+r_4)(b-y+r_2)}\right] \quad (22)$$

where r_1, r_2, r_3, and r_4 represent the distances from the field point to the four corners of the rectangular coil, expressed as follows:

$$r_1 = \sqrt{(x-a)^2 + (y-b)^2 + z^2}$$
$$r_2 = \sqrt{(x+a)^2 + (y-b)^2 + z^2}$$
$$r_3 = \sqrt{(x+a)^2 + (y+b)^2 + z^2}$$
$$r_4 = \sqrt{(x-a)^2 + (y+b)^2 + z^2}. \quad (23)$$

Similarly, introduce a new set of electromagnetic parameters I_c and μ_c, and such that $\boldsymbol{A}_{c\pm} = \boldsymbol{A}_{a-}$. Let $\mu_c = \mu_0$; then, the magnetic vector potential on the boundary interface S_c can be computed as follows:

$$A_{cx\pm} = \frac{\mu_0 I}{4\pi} \ln\left[\frac{(-a-x+r_2)(a-x+r_4)}{(a-x+r_1)(-a-x+r_3)}\right] + \frac{\mu_0 I_c}{4\pi} \ln\left[\frac{(-a-x+r_2)(a-x+r_4)}{(a-x+r_1)(-a-x+r_3)}\right]$$
$$A_{cy\pm} = \frac{\mu_0 I}{4\pi} \ln\left[\frac{(b-y+r_1)(-b-y+r_3)}{(-b-y+r_4)(b-y+r_2)}\right] + \frac{\mu_0 I_c}{4\pi} \ln\left[\frac{(b-y+r_1)(-b-y+r_3)}{(-b-y+r_4)(b-y+r_2)}\right]. \quad (24)$$

Taking the curl of (22) and (24) yields the magnetic flux density distributions on S_b and S_c, respectively. According to Maxwell's equations, the magnetic flux density relationship at the interface in Fig. 5(a) can be expressed as follows:

$$B_{az-} = B_{az+}$$

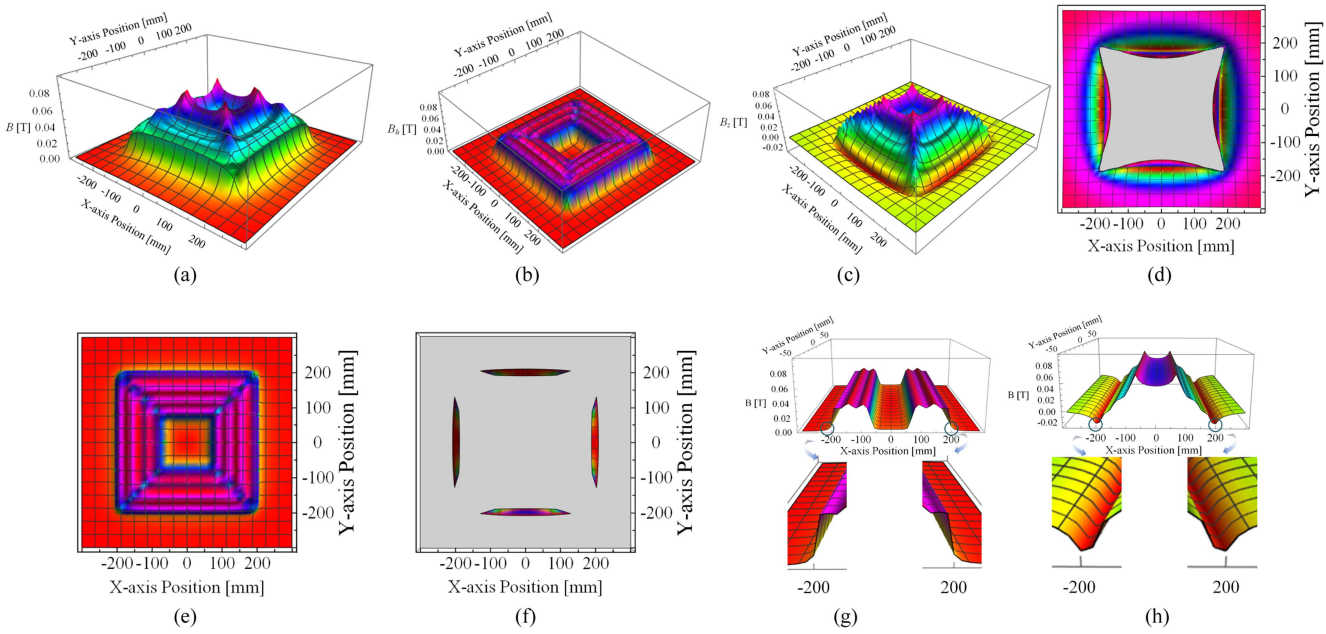

Fig. 6. Magnetic field distribution inside the core (located at the lower surface of the core). (a) Magnetic flux density B. (b) Horizontal component B_h. (c) Vertical component B_z. (d) Region where magnetic field lines emerge from the core (colored). (e) and (g) Top view of B_h and local magnification of details. (f) and (h) Main region where magnetic field lines emerge and local magnification of B_z details.

$$H_{ax-} = H_{ax+}$$
$$H_{ay-} = H_{ay+}. \tag{25}$$

By substituting (22) and (24) into (25), the relationship between I_b and I can be derived as follows:

$$I_{\mathrm{b}} = \frac{2\mu_0}{\mu_0 + \mu_r \mu_0} I. \tag{26}$$

By substituting (26) into (22), the magnetic field distribution inside the magnetic core can be obtained as follows:

$$B_x = \frac{\mu_0 \mu_r I}{2\pi (1+\mu_r)} \sum_{i=1}^{4} \left[\frac{(-1)^i z}{r_i (M_i + r_i)} \right]$$
$$B_y = \frac{\mu_0 \mu_r I}{2\pi (1+\mu_r)} \sum_{i=1}^{4} \left[\frac{(-1)^i z}{r_i (N_i + r_i)} \right]$$
$$B_z = \frac{\mu_0 \mu_r I}{2\pi (1+\mu_r)} \sum_{i=1}^{4} \left[\frac{(-1)^i N_i}{r_i (M_i + r_i)} + \frac{(-1)^i M_i}{r_i (N_i + r_i)} \right] \tag{27}$$

where $M_1 = M_2 = b - y$, $M_3 = M_4 = -b - y$, $N_1 = N_4 = a - x$, $N_2 = N_3 = -a - x$.

Under the condition that other factors remain unchanged, the magnetic field distribution on the bottom surface of the magnetic core governs the magnetic field distribution within the coupling region. By substituting the coil parameters from Table I into (27) and using JF95 (with a relative permeability of 3300) as the magnetic core material, the magnetic flux density B, horizontal component B_h, and vertical component B_z distributions on the bottom surface of the magnetic core (still within the core) were obtained for an excitation current of 30 A. The results are presented in Fig. 6(a)–(c). The x- and y-axes represent the position coordinates along their respective directions, with the center of the magnetic core defined as the midpoint of the x-y plane. The findings show that the magnetic flux density B within the core is minimal at the center, increasing and subsequently decreasing in a "saddle" shape as the region extends outward. Fig. 6(d) highlights the color region where B_z is less than 0, indicating that the magnetic flux lines exit the core, thereby enhancing coupling. As depicted in Fig. 6(e)–(h), an interesting region exists where the horizontal magnetic field component B_h decreases sharply, and the direction of the vertical component B_z undergoes a transition. Moreover, at the boundary of a square with a side length of 400 mm, the rate of change of the horizontal magnetic field component experiences a discontinuity. As the boundary size increases, the horizontal component decreases very slowly, while the vertical component B_z reverses and increases to its maximum. This behavior suggests that this region is where the primary magnetic flux predominantly exits the core.

The influence of the magnetic core on the system is generated through magnetization. As the core size increases, the total magnetization of the core increases at a gradually slower rate. Once the size exceeds a certain threshold, the outer core material becomes nearly nonmagnetized, and the system's transmission capacity remains almost unchanged. In addition, the internal losses of the core are positively correlated with the magnetic flux density. This method can also be used to predict the distribution pattern of the core's internal losses.

Based on the theoretical analysis of the magnetic field distribution within the core, an IPT system was constructed using the parameters listed in Table I. Three types of magnetic cores were designed: an optimally sized core (L = 400 mm), an oversized reference core (L = 500 mm), and an undersized reference core (L = 300 mm). Theoretical analysis predicts that as the magnetic core size of the system increases up to 400 mm, the transmission efficiency improves significantly, and

TABLE II
SIMULATION PARAMETERS OF MAGNETIC CORE MATERIAL

Parameters	Value
Coil Conductivity (10^7S•m^{-1})	5.998
Coil Density (g•cm^{-3})	8.9
Distance Between Magnetic Core and Coil (mm)	5
Current Frequency (kHz)	85
Ferrite Thickness (mm)	5
Relative Permeability of Ferrite	3300
Ferrite Density (kg•m^{-3})	4900
Ferrite Density (Ω•m)	8.5
Thermal Conductivity of Ferrite	0.035

the magnetic-thermal balance becomes more favorable. However, when the core size exceeds 400 mm, further increases yield negligible improvements in transmission efficiency, with the magnetic-thermal characteristics remaining nearly unchanged. In the following sections, the energy efficiency performance of three representative core sizes will be evaluated through simulation and experimental analysis to validate the effectiveness of the proposed core size optimization method.

III. FINITE ELEMENT SIMULATION ANALYSIS

The frequency-domain simulation model of the three-dimensional magnetic coupling mechanism is developed using the coil parameters presented in Table I and the core parameters provided in Table II.

As a classical loss evaluation method under sinusoidal excitation, the Steinmetz formula is chosen to assess the core loss P of the IPT system. The power loss per unit volume can be expressed by the following formula [21]:

$$P = kf^{\partial}B_m^{\beta} \tag{28}$$

where k, α, and β are the Steinmetz parameters. The values of these parameters are related to the material properties and are typically obtained from material databases. In this study, the parameters are determined by fitting experimental data. f represents the excitation frequency, and B_m is the amplitude of the sinusoidal excitation. In this study, P is treated as the heat source for the subsequent magnetic-thermal coupling analysis.

Fig. 7 illustrates the distribution of transmitter-side core loss P under an operating frequency of 85 kHz for three magnetic core configurations: the optimally sized core ($L = 400$ mm), the oversized reference core ($L = 500$ mm), and the undersized reference core ($L = 300$ mm), at power transfer levels of 5 and 11.1 kW. The results show that the loss is primarily concentrated within a rectangular region with a side length of approximately 400 mm. As the observation point moves from the center toward the edge, the loss distribution exhibits a "saddle-shaped" profile—first increasing, then decreasing—which is consistent with the previously derived magnetic field distribution pattern. At a transfer power of 5 kW, the undersized core exhibits the highest loss density, approximately 1.24×10^5 W/m^3, significantly higher than that of the optimally sized core (8.82×10^4 W/m^3). At 11.1 kW, the loss distribution for the oversized core (1.82×10^5 W/m^3) is nearly identical to that of the optimal core (1.64×10^5 W/m^3).

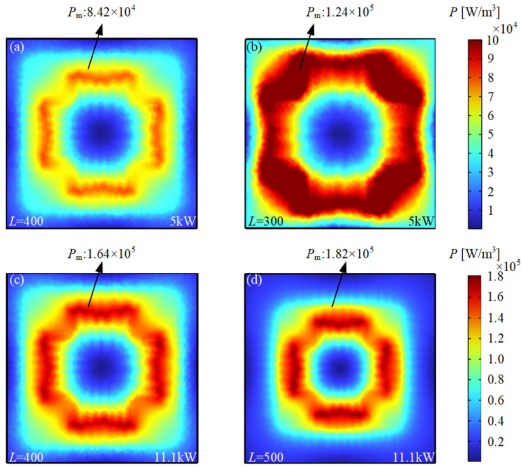

Fig. 7. (a)–(d) Simulated core loss density P distributions for magnetic cores with lengths $L = 300$ mm, $L = 400$ mm, and $L = 500$ mm throughout the entire magnetic core under different transmitted power levels.

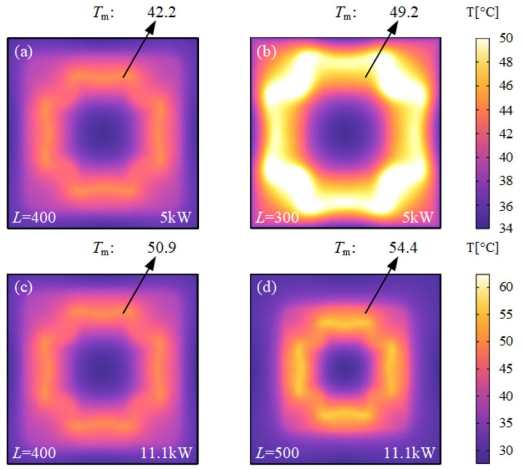

Fig. 8. (a)–(d) Simulated core surface temperature T distributions for magnetic cores with lengths $L = 300$ mm, $L = 400$ mm, and $L = 500$ mm under different transmitted power levels.

These simulation results validate the effectiveness of the proposed core size optimization methodology.

Fig. 8 presents the temperature distributions of the three core configurations under power transfer levels of 5 and 11.1 kW. The temperature profiles exhibit a "saddle-shaped" pattern similar to that of the core loss density, which is expected given that heat generation in the core is primarily due to magnetic core loss. It can be observed that the oversized reference core and the optimally sized core exhibit very similar thermal distributions, with comparable peak temperatures. In contrast, the undersized core exhibits significantly higher temperature rise under the same power level. This phenomenon can be explained by the distribution of magnetic field lines within the core, as illustrated in Fig. 9. When the core is undersized, an equivalent opposing magnetic field may be induced relative to the main flux, resulting in a shortened horizontal transmission path and causing the flux to exit the core prematurely. This behavior leads to a reduction in system inductance and transmission efficiency. In addition, the boundary effect leads to an increase in the normal component

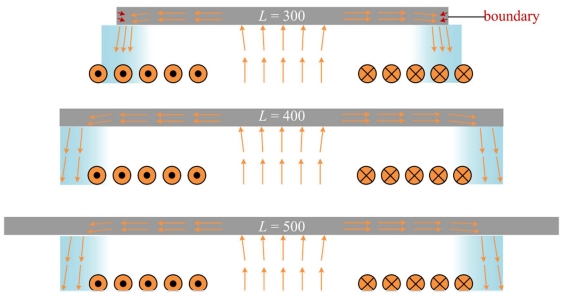

Fig. 9. Influence of core sizes on internal magnetic flux distribution.

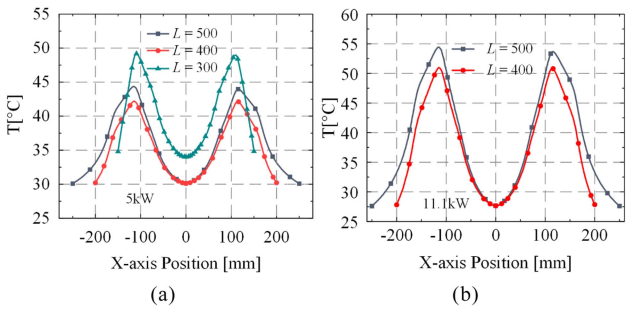

Fig. 10. Temperature T distribution along the X-axis of the core surface.

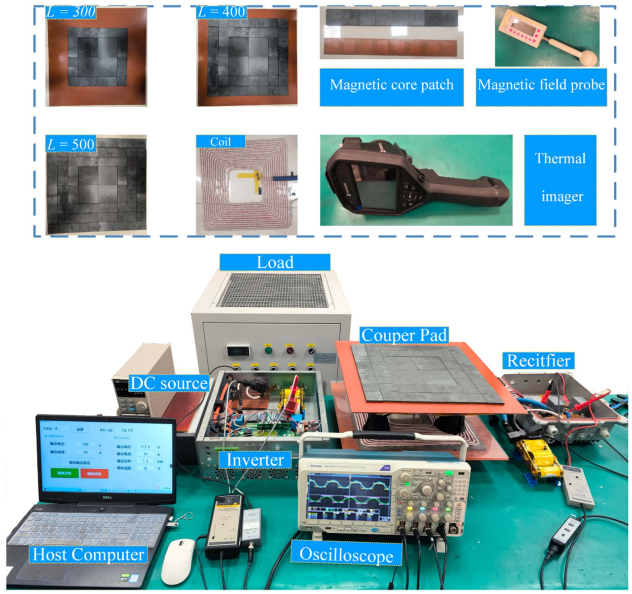

Fig. 11. Photograph of the 11.1-kW IPT prototype with adjustable switching frequency from 10 to 100 kHz.

of the magnetic field within the horizontal transmission region, resulting in a local rise in the total magnetic field intensity and consequently increased localized losses.

To further clarify the influence of core size on thermal performance, a two-dimensional Cartesian coordinate system was established with the center of the core as the origin. The relationship between the surface temperature and position for the experimental and reference groups is illustrated in Fig. 10. It is observed that the peak temperature of the undersized reference core occurs at $x = -110$ and 110 mm, whereas for both the optimally sized and oversized cores, the peak appears at $x = -115$ and 115 mm, indicating an earlier emergence of the maximum heating point in the undersized configuration. Moreover, the maximum temperature of the undersized core is significantly higher than that of the other two cores. In contrast, the temperature distributions of the optimally sized and oversized cores are nearly identical. When the core size is below a critical threshold, increasing the core dimension under the same power transfer condition can effectively mitigate heat generation. However, once the core reaches this threshold, further enlarging the size yields negligible improvements in either core loss or thermal performance. In addition, it is noted that the heat-affected region of the undersized core is primarily concentrated in the four corners, a phenomenon not observed in the other two configurations. This behavior may be attributed to edge effects, where the magnetic flux lines, influenced by the core's geometry, become more concentrated at the corners, resulting in localized overheating. These findings further emphasize the necessity of proper core size design.

IV. Experimental Verification of Transmission Efficiency and Thermal Performance

A. Experimental Platform Description for 11.1 kW IPT System

To validate the accuracy of the simulation results and the effectiveness of the proposed core design methodology, it is essential to experimentally evaluate the ac–ac transmission efficiency and thermal performance of the IPT system using the three square magnetic cores. Based on the simulation model, an experimental platform was constructed for an 11.1-kW IPT system with adjustable operating frequency ranging from 10 to 100 kHz, as shown in Fig. 11. The 11.1-kW IPT prototype system consists of a dc power supply, inverter, series compensation circuit, transmitter core, coupling coils, receiver core, series compensation circuit, rectifier, load, and oscilloscope. In addition, the IPT system is equipped with a custom-developed frequency control unit that enables real-time regulation of the operating frequency. The magnetic coupling coils are wound using USGC 0.1 mm $\times$ 1800 litz wire, and the magnetic cores are assembled from JF95 core segments.

The inverter of the prototype is a self-designed module, which includes the main control board G201_V3.0, display board G202_LCD_V3, driver board G203_V3.1, and auxiliary power supply board G205B_V3.0. The rectifier is also a self-developed GS201A_V2.0 module, with the electronic load model RXF-750V-25R and the oscilloscope model DSO-X 3034A. The capacitors are film capacitors of model DAWN-CAP DTR, 3000 V/60 A (Tianming Corporation, Suzhou, China). Current and voltage signals in the circuit are collected through high-frequency current loops and voltage probes, which are then input into the oscilloscope for real-time monitoring. At the same time, signals from both the rectifier and inverter ends are transmitted in real-time to the upper-level computer for feedback and

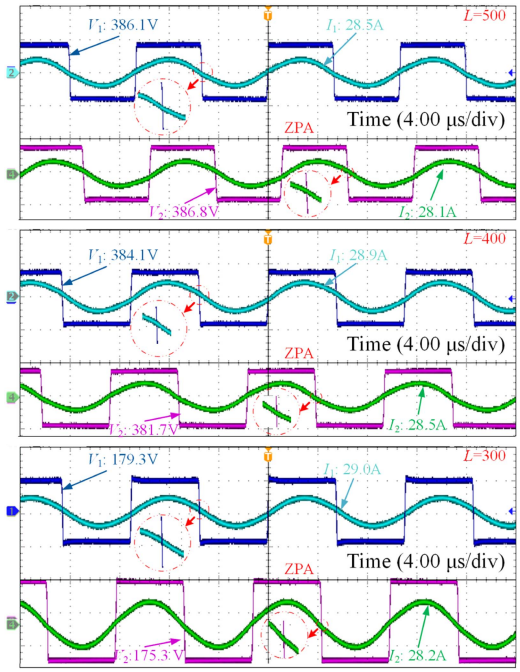

Fig. 12. Steady-state waveforms of input voltage V_1, input current I_1, output voltage V_2, and output current I_2 of the IPT system under different core lengths: $L = 300$ mm, $L = 400$ mm, and $L = 500$ mm.

TABLE III
EXPERIMENTAL PARAMETERS

Parameters	$L = 300$	$L = 400$	$L = 500$
L_1	74.5 μH	93.1 μH	99.0 μH
L_2	72.7 μH	91.6 μH	97.1 μH
M	14.7 μH	22.3 μH	25.5 μH
k	0.20	0.24	0.26
C_1	47.3 nF	37.9 nF	35.6 nF
C_2	48.5 nF	38.5 nF	36.3 nF
f	85 kHz	85 kHz	85 kHz
d	170 mm	170 mm	170 mm

adjustment. To ensure the accuracy of the system's energy efficiency performance testing, high-frequency current loops, models HDWA100 and HDWA150, are used for current collection.

To ensure consistency in the research subjects and facilitate performance comparison while reducing system reactive power loss, this study adopts the S-S circuit topology. Fig. 12 presents the steady-state waveforms of the input voltage V_1, input current I_1, output voltage V_2, and output current I_2, for the IPT systems configured with the three magnetic core types at the designated operating point. After aligning the phase angle between V_1 and I_1, as well as between V_2 and I_2, the operating frequency was fine-tuned to achieve zero-phase angle conditions at both input and output sides, thereby enabling soft-switching operation across the entire charging system.

The key experimental parameters are shown in Table III, where the subscript 1 represents the self-inductance and compensation capacitance of the transmitter, and the subscript 2 represents the self-inductance and compensation capacitance of the receiver. The symbol "d" denotes the air gap length between the magnetic cores of the transmitter and receiver.

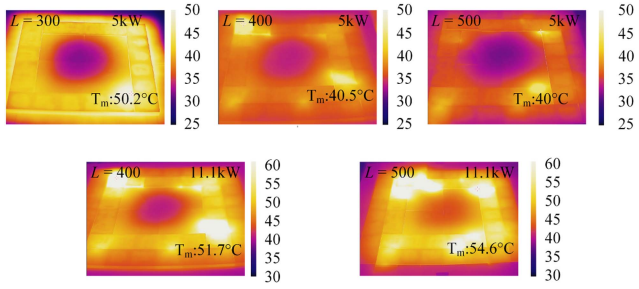

Fig. 13. Temperature T distributions of magnetic cores with lengths $L = 300$ mm, $L = 400$ mm, and $L = 500$ mm at 85 kHz.

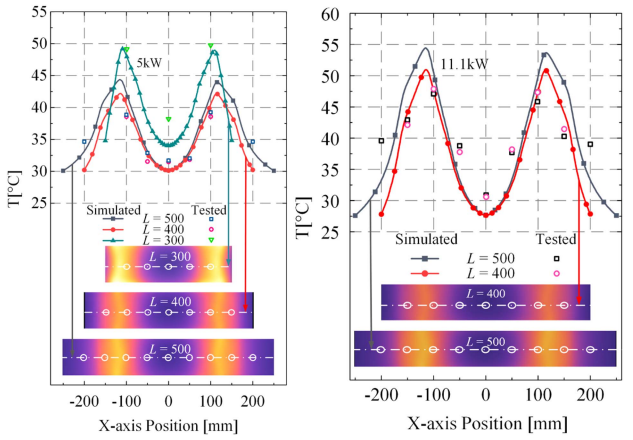

Fig. 14. Comparison of simulated and measured temperature values along the X-axis of magnetic core surface with lengths $L = 300$ mm, $L = 400$ mm, and $L = 500$ mm at 85 kHz.

B. Thermal Performance and AC–AC Transmission Efficiency

To compare and analyze the thermal characteristics of the three magnetic cores, the system is assumed to be in a steady-state condition once the temperature on the core surface stabilizes. An infrared thermal imager is employed to capture the temperature distribution across the entire core.

Fig. 13 shows the temperature profiles of the cores under steady-state operation. Under a transmitter-side power of 5 kW, the maximum surface temperature of the small reference core reaches 50.2 °C, which is significantly higher than that of the optimal-sized core (40.5 °C) and the large reference core (40 °C). At 11.1 kW, the temperature distributions of the optimal-sized and large reference cores are nearly identical. Fig. 14 presents a comparison between the simulated and measured temperatures at selected surface points of the core under steady-state conditions. The deviation at the maximum temperature point between the simulation and experimental results is less than 5% .The temperature gradient across the small reference core is 15.2 °C, which is notably higher than that of the optimal-sized core (6.9 °C) and the large reference core (7.5 °C). The results show that the thermal performance of the large reference core is comparable to that of the optimally sized core, whereas the small reference core exhibits significantly more severe heat generation.

The ac–ac efficiency in this work is defined as the ratio of the rectifier input energy to the inverter output energy, and is given

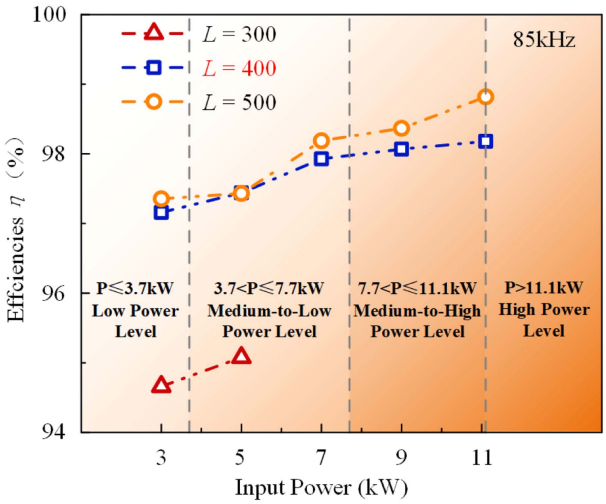

Fig. 15. AC–AC transmission efficiencies η of the IPT system with core lengths $L = 300$ mm, $L = 400$ mm, and $L = 500$ mm under varying transmitted power levels at 85 kHz.

by the following equation:

$$\eta = \frac{U_{2m} I_{2r} \cos\theta_2}{U_{1m} I_{1r} \cos\theta_1} \tag{29}$$

where U_{2m} and U_{1m} are the amplitudes of the square-wave voltages at the receiving and transmitting sides, respectively; I_{2r} and I_{1r} are the rms values of the sinusoidal currents; and θ_2 and θ_1 denote the phase differences between voltage and current at the receiving and transmitting sides, respectively. The efficiency was measured and calculated using an oscilloscope.

Fig. 15 shows the ac–ac power transfer efficiency of the IPT systems equipped with the three magnetic cores under an 85 kHz operating frequency, with transfer power ranging from 3 to 11.1 kW. The results indicate that the system's efficiency improves as the power level increases. Throughout the power ramp-up process, the transfer efficiencies of the optimally sized core and the oversized reference core remain nearly identical, with a maximum deviation of only 0.6% . At a transmission power of 11.1 kW, the efficiencies of the optimally sized and oversized cores reach 98.2% and 98.8%, respectively. In addition, when the transmission power reaches 5 kW, the current on the transmitter side for the undersized core already reaches 28.2 A. Considering the current-handling capability of the coils and the safety constraints of the experimental equipment, the transmission power of the undersized core was not increased further. Its maximum observed efficiency was 95.1% .

Due to the magnetic core size not reaching the threshold, the small control group core (with a coupling coefficient of 0.20) faces difficulty in improving power levels compared to the optimal core size (with a coupling coefficient of 0.24) and the large control group (with a coupling coefficient of 0.26). Therefore, under the same power conditions, the small control group has a higher current. In the actual experimental process, we made every effort to ensure that the magnetic core designed based on the magnetic field distribution rule has the same current as the large control group core at different power levels, for experimental validation. The ac resistance of the coils under 85 kHz conditions was tested using an impedance analyzer, with

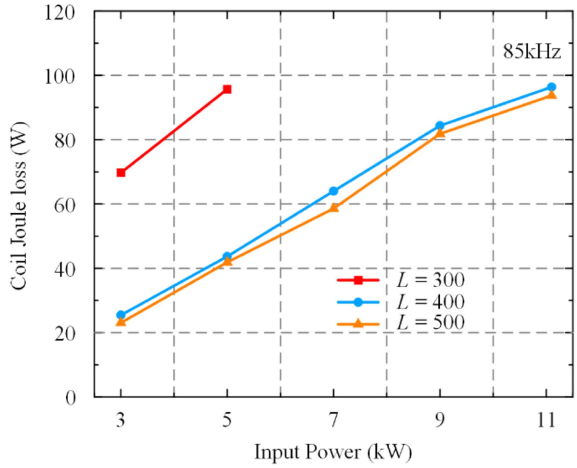

Fig. 16. Joule losses in the litz wire.

the transmitter coil resistance being 0.059 Ω and the receiver coil resistance being 0.056 Ω. The Joule losses in the coils under different power levels are shown in Fig. 16.

At an input power level of 11.1 kW, an efficiency difference of 0.6% is non-negligible [22]. For such a power level, transmission efficiency and power density are critical performance metrics. To facilitate a direct comparison of the energy efficiency characteristics of magnetic cores under high-power conditions, an evaluation function is defined as in the following equation:

$$S = \frac{\eta W}{L^2 d} \tag{30}$$

where η denotes the ac–ac efficiency, W is the output energy of the inverter, L is the side length of the core, and d is the distance between the lower surface of the transmitting core and the upper surface of the receiving core. The mathematical meaning of this evaluation function is the product of transmission efficiency and power density. Therefore, a larger value of the function indicates a greater advantage of the magnetic core in terms of energy efficiency.

In the calculation, the unit of energy is chosen as watt and the unit of length as meter. Under the 11.1-kW condition, the value of the evaluation function is 378 496.2 for the 400-mm core system, compared with 243 792.3 for the 500-mm core system. This result demonstrates the superior energy-efficiency performance of the 400-mm core under high-power operation.

From the perspective of transfer efficiency, the results confirm that, within a certain range, increasing the magnetic core size leads to improved efficiency. However, once the core size exceeds a critical threshold, further enlargement yields negligible gains. Moreover, if the core size is below this threshold, the system may be unable to support higher transmission power levels.

Compared with the theoretically designed core, the large reference core—with a 25% increase in side length and a 56.2% increase in area—yields only a 0.6% improvement in transmission efficiency. In contrast, the small reference core—with a 25% reduction in side length and a 43.8% reduction in area—results in a 3% decrease in transmission efficiency, while the optimally sized core achieves both improved efficiency and a significant reduction in heat generation. These results indicate

TABLE IV
COMPARISON AND SUMMARY OF THIS STUDY WITH MULTIOBJECTIVE OPTIMIZATION METHODS

Optimization Methods	Multi-Objective Optimization	The Methodology of This Study
Advantages	Effective solution when multiple design objectives (such as performance, cost, volume, material selection, magnetic leakage shielding, etc.) need to be considered simultaneously.	Simple and effective calculation method, fast computation speed, minimal computational resources, and provides intuitive understanding.
Disadvantages	Requires extensive simulation calculations and algorithm iterations, making computational resources and time consumption a significant challenge [26].	Simplified the actual model, resulting in limited accuracy, and can only be used to analyze planar coil models.
Applicability	Applicable to design problems involving multiple conflicting objectives.	Applicable to real-time calculations or scenarios requiring frequent estimations.
Reference	[1][10][11][27][28]	This work

the existence of a threshold in core dimensions, beyond which further increases produce negligible gains in transmission efficiency and magneto-thermal performance. The proposed design method effectively identifies this threshold and validates the effectiveness of using analytical magnetic field distribution to guide core sizing.

C. Discussion

The proposed approach for evaluating the core dimension threshold relies on the distribution of the horizontal component of the magnetic flux density within the core. It is therefore necessary to assess whether the finite thickness of the core has a significant influence on this distribution. Taking the receiver-side magnetic core in Fig. 2 as an example, the leakage flux above the top surface of a finite-thickness core is negligible compared with the dominant flux inside the core. Hence, the top surface can be reasonably treated as a magnetic insulation boundary with nearly zero flux, which introduces a symmetric boundary condition. Under this condition, the magnetic flux density inside the core can be represented as the superposition of the fields generated by two equivalent coils, whose horizontal components are aligned in the same direction. Since the geometric structures are identical, their attenuation behavior is also identical. This indicates that the effect of core thickness on the horizontal component is mainly reflected in its magnitude, while the attenuation location remains unaffected. Consequently, neglecting the core thickness in the analysis of the core dimension threshold is a justified and effective simplification.

To better highlight the contributions of this study, a comparative summary between this research and the mainstream multiobjective optimization methods in current magnetic core design is provided, as shown in Table IV.

Thanks to the rapid development of finite element simulation software, multiobjective optimization has become the mainstream method in current magnetic core optimization research [23], [24], [25]. However, this does not mean that the analytical algorithm used in this study has lost its applicability. The approach in this study requires fewer computational resources, offers fast computation speed, and provides explicit calculation formulas, making it suitable for real-time calculations or scenarios that require frequent estimations. Furthermore, this study can complement numerical calculations, collectively advancing the research in IPT system magnetic core optimization.

V. CONCLUSION

This article proposes an analytical method for characterizing the internal magnetic field distribution within the pad, aiming to determine the optimal pad size for IPT systems. By examining the influence of core permeability on coil inductance, a critical phenomenon is observed: as the magnetic performance of the pad increases, the power transfer capability of the IPT system improves accordingly. However, once the pad performance exceeds a certain threshold, further enhancement yields negligible improvements in transmission performance.

It is observed that the pad size is a critical parameter in magnetic pad design, as it directly affects both the power density and transmission efficiency of the IPT system. Based on the proposed analytical method for evaluating the internal magnetic field distribution, a threshold for pad size is identified to guide optimal pad sizing. This design approach effectively addresses the issues associated with undersized pads, such as insufficient transmission efficiency and excessive thermal buildup, as well as the decline in power density caused by oversized pads. As a result, the method enables efficient pad utilization and facilitates the design of IPT systems with high power density.

The proposed pad size design method has been applied to both simulation models and an 11.1-kW IPT system prototype. Compared with the theoretically designed pad, the large reference pad—with a 25% increase in side length and a 56.2% increase in area—achieves only a 0.6% improvement in ac–ac transmission efficiency. In contrast, the optimally sized pad improves transmission efficiency by 3% and reduces the maximum temperature by 10 °C compared to the small reference pad, which has a 25% reduction in side length and a 43.8% reduction in area.

APPENDIX

1) For an IPT system operating under magnetostatic field conditions, the magnetic field components and electric field components in all regions satisfy the following conditions

$$\nabla \times \boldsymbol{B} = \mu_0 \mu_r \boldsymbol{J} \tag{A1}$$

$$\boldsymbol{J} = \gamma \boldsymbol{E} \tag{A2}$$

$$\nabla \times \boldsymbol{E} = -\frac{\partial \boldsymbol{B}}{\partial t}. \tag{A3}$$

The coil current in the IPT system can be approximated as a sinusoidal current. By taking the curl of (A1) and transforming

the bi-curl equation into the Laplace equation, a partial differential equation that only contains the magnetic flux density $\boldsymbol{B}$ is obtained, as shown in (3).

The magnetic vector potential of the current-carrying rectangular coil in space can be calculated using (4). The calculation process in the frequency domain is as follows:

$$\begin{aligned}\boldsymbol{a_t}(\omega_1,\omega_2,z) &= \frac{\mu_0 I}{4\pi}\oint_l\left[\int_{-\infty}^{+\infty}\int_{-\infty}^{+\infty}\right.\\ &\left.\times\frac{e^{-j(x\omega_1+y\omega_2)}}{\sqrt{(x-x')^2+(y-y')^2+(z-z_0)^2}}dxdy\right]d\boldsymbol{l'}\\ &= \frac{\mu_0 I}{2}\frac{e^{-|z-z_0|\sqrt{{\omega_1}^2+{\omega_2}^2}}}{\sqrt{{\omega_1}^2+{\omega_2}^2}}\oint_l e^{-j(x'\omega_1+y'\omega_2)}d\boldsymbol{l'}.\end{aligned} \tag{A4}$$

By considering the geometric shape and spatial position of the coil, the frequency-domain components of the magnetic vector potential and the magnetic field can be calculated. The frequency-domain magnetic field components $\boldsymbol{b_t}$ are calculated as shown in (9) as follows:

$$\begin{aligned} b_{t\omega_1} &= \frac{j2\mu_0 I\sin(x_0\omega_1)\sin(y_0\omega_2)}{\omega_2}e^{(z_0-z)\sqrt{{\omega_1}^2+{\omega_2}^2}}\\ b_{t\omega_2} &= \frac{j2\mu_0 I\sin(x_0\omega_1)\sin(y_0\omega_2)}{\omega_1}e^{(z_0-z)\sqrt{{\omega_1}^2+{\omega_2}^2}}\\ b_{tz} &= \frac{2\mu_0 I\sqrt{{\omega_1}^2+{\omega_2}^2}\sin(x_0\omega_1)\sin(y_0\omega_2)}{\omega_1\omega_2}\\ &\quad\times e^{(z_0-z)\sqrt{{\omega_1}^2+{\omega_2}^2}}. \end{aligned} \tag{A5}$$

Therefore, for the magnetic field generated by a planar rectangular magnetic source, its frequency-domain form can be obtained by solving only the z-component. The expressions for the other components can then be derived using (A5).

The magnetic flux density $\boldsymbol{B_n}$ in other regions also satisfies (3). By applying the Fourier transform to (3), the frequency-domain control equation satisfied by $\boldsymbol{b_n}$ is obtained as follows:

$$\frac{\partial^2 \boldsymbol{b_n}}{\partial z^2} = \left(j\omega\mu_0\mu_r\gamma+\omega_1^2+\omega_2^2\right)\boldsymbol{b_n} \tag{A6}$$

where $n = 1, 2, 5, 6$.

Although (A6) is a second-order partial differential equation, it only contains second-order partial derivatives with respect to z. Therefore, it can be treated as an ordinary differential equation for b_{nz} and solved accordingly. The general solution is given by

$$b_{nz} = C_{nz}e^{\sqrt{j\omega\mu_0\mu_n\gamma_n+\omega_1^2+\omega_2^2}z}+C'_{nz}e^{-\sqrt{j\omega\mu_0\mu_n\gamma_n+\omega_1^2+\omega_2^2}z}. \tag{A7}$$

Specifically, for regions 1 and 6, based on the magnetic field distribution characteristics, we obtain $C_{6z} = 0$ and $C'_{1z} = 0$. Therefore, there are a total of eight unknown coefficients: C_{1z}, C_{2z}, C'_{2z}, C_{iz}, C'_{iz}, C_{5z}, C'_{5z}, C'_{6z}. Solving for these coefficients requires solving the following system of equations:

$$\begin{cases} b_{tz}+b_{iz} = b_{2z}\,(z=0) & b_{1z} = b_{2z}\,(z=-t)\\ b_{tz}+b_{iz} = b_{5z}\,(z=d) & b_{5z} = b_{6z}\,(z=d+t)\\ b_{tx}+b_{ix} = \frac{b_{2x}}{\mu_2}\,(z=0) & b_{1x} = \frac{b_{2x}}{\mu_2}\,(z=-t)\\ b_{tx}+b_{ix} = \frac{b_{5x}}{\mu_5}\,(z=d) & b_{6x} = \frac{b_{5x}}{\mu_5}\,(z=d+t)\end{cases}. \tag{A8}$$

Substituting the specific expressions, we obtain

$$\begin{cases} C_{tz}e^{-2\lambda s_1}+C_{iz}+C'_{iz} = C_{2z}+C'_{2z}\\ C_{1z}e^{-\lambda t} = C_{2z}e^{-\lambda' t}+C'_{2z}e^{\lambda' t}\\ C_{tz}e^{-\lambda d}+C_{iz}e^{\lambda d}+C'_{iz}e^{-\lambda d} = C_{5z}e^{\lambda' d}+C'_{5z}e^{-\lambda' d}\\ C_{5z}e^{\lambda'(d+t)}+C'_{5z}e^{-\lambda'(d+t)} = C'_{6z}e^{\lambda(d+t)}\\ \frac{\omega_1}{j\lambda}\left(C_{tz}e^{-2\lambda s_1}+C_{iz}-C'_{iz}\right) = \frac{\omega_1}{j\mu_2\lambda}\left(C_{2z}-C'_{2z}\right)\\ \frac{\omega_1}{j\lambda}C_{1z}e^{-\lambda t} = \frac{\omega_1}{j\mu_2\lambda}\left(C_{2z}e^{-\lambda' t}-C'_{2z}e^{\lambda' t}\right)\\ \frac{\omega_1}{j\lambda}\left(C_{tz}e^{-\lambda d}+C_{iz}e^{\lambda d}-C'_{iz}e^{-\lambda d}\right)\\ \qquad = \frac{\omega_1}{j\mu_5\lambda}\left(C_{5z}e^{\lambda' d}-C'_{5z}e^{-\lambda' d}\right)\\ \frac{\omega_1}{j\lambda}C'_{6z}e^{\lambda(d+t)} = \frac{\omega_1}{j\mu_5\lambda}\left(C_{5z}e^{\lambda'(d+t)}-C'_{5z}e^{-\lambda'(d+t)}\right)\end{cases} \tag{A9}$$

where λ and λ' are the characteristic roots of (A6) in different regions, with the specific expressions given as follows:

$$\begin{aligned}\lambda &= \sqrt{{\omega_1}^2+{\omega_1}^2}\\ \lambda' &= \sqrt{j\omega\mu_0\mu_r\gamma+{\omega_1}^2+{\omega_1}^2}.\end{aligned} \tag{A10}$$

For the calculation of the z-component of the magnetic field at a point in the coupling region, the formula (18) requires numerical integration using mathematical software. The coil inductance can be obtained by fitting the sampled points into a surface and then performing a surface integral.

REFERENCES

[1] R. Dou et al., "Nanocrystalline power loss and thermal mitigation for 11.1 kW inductive power transfer pads: A novel frequency-dependent optimization," *IEEE Trans. Power Electron.*, vol. 40, no. 1, pp. 2513–2526, Jan. 2025.

[2] P. Zhang et al., "Dual-layer equalization architecture for antimisalignment capability enhancement in multiple-receiver-based WPT equalizer," *IEEE Trans. Power Electron.*, vol. 39, no. 10, pp. 14027–14038, Oct. 2024.

[3] K. Clement-Nyns, E. Haesen, and J. Driesen, "The impact of charging plug-in hybrid electric vehicles on a residential distribution grid," *IEEE Trans. Power Syst.*, vol. 25, no. 1, pp. 371–380, Feb. 2010.

[4] U. K. Madawala and D. J. Thrimawithana, "A bidirectional inductive power interface for electric vehicles in V2G systems," *IEEE Trans. Ind. Electron.*, vol. 58, no. 10, pp. 4789–4796, Oct. 2011.

[5] C. Liu, K. T. Chau, D. Wu, and S. Gao, "Opportunities and challenges of vehicle-to-home, vehicle-to-vehicle, and vehicle-to-grid technologies," *Proc. IEEE*, vol. 101, no. 11, pp. 2409–2427, Nov. 2013.

[6] F. Y. Lin, G. A. Covic, and J. T. Boys, "Evaluation of magnetic pad sizes and topologies for electric vehicle charging," *IEEE Trans. Power Electron.*, vol. 30, no. 11, pp. 6391–6407, Nov. 2015.

[7] T. Yilmaz, N. Hasan, R. Zane, and Z. Pantic, "Multi-objective optimization of circular magnetic couplers for wireless power transfer applications," *IEEE Trans. Magn.*, vol. 53, no. 8, Aug. 2017, Art. no. 8700312.

[8] C. Jiang, X. Li, S. S. Ghosh, H. Zhao, Y. Shen, and T. Long, "Nanocrystalline powder cores for high-power high-frequency power electronics applications," *IEEE Trans. Power Electron.*, vol. 35, no. 10, pp. 10821–10830, Oct. 2020.

[9] Z. Luo, X. Li, C. Jiang, and T. Long, "Characterization of nanocrystalline flake ribbon for high frequency magnetic cores," *IEEE Trans. Power Electron.*, vol. 37, no. 12, pp. 14011–14016, Dec. 2022.

[10] B. S. Gu, T. Dharmakeerthi, S. Kim, M. J. O'Sullivan, and G. A. Covic, "Optimized magnetic core layer in inductive power transfer pad for electric vehicle charging," *IEEE Trans. Power Electron.*, vol. 38, no. 10, pp. 11964–11973, Oct. 2023.

[11] Z. Luo, X. Wei, M. G. S. Pearce, and G. A. Covic, "Multiobjective optimization of inductive power transfer double-D pads for electric vehicles," *IEEE Trans. Power Electron.*, vol. 36, no. 5, pp. 5135–5146, May 2021.

[12] W. Zhang, Q. Yang, Y. Li, Z. Lin, M. Yang, and M. Mi, "Comprehensive analysis of nanocrystalline ribbon cores in high-power-density wireless power transfer pads for electric vehicles," *IEEE Trans. Magn.*, vol. 58, no. 2, Feb. 2022, Art. no. 8700605.

[13] J. Acero, C. Carretero, I. Lope, R. Alonso, Ó. Lucia, and J. M. Burdio, "Analysis of the mutual inductance of planar-lumped inductive power

transfer systems," *IEEE Trans. Ind. Electron.*, vol. 60, no. 1, pp. 410–420, Jan. 2013.
[14] Z. Luo and X. Wei, "Analysis of square and circular planar spiral coils in wireless power transfer system for electric vehicles," *IEEE Trans. Ind. Electron.*, vol. 65, no. 1, pp. 331–341, Jan. 2018.
[15] Z. Luo, S. Nie, M. Pathmanathan, W. Han, and P. W. Lehn, "3-D analytical model of bipolar coils with multiple finite magnetic shields for wireless electric vehicle charging systems," *IEEE Trans. Ind. Electron.*, vol. 69, no. 8, pp. 8231–8242, Aug. 2022.
[16] Z. Chen, Z. Li, Z. Lin, J. Li, and Y. Zhang, "Mutual inductance calculation of rectangular coils at arbitrary position with bilateral finite magnetic shields in wireless power transfer systems," *IEEE Trans. Power Electron.*, vol. 39, no. 10, pp. 14065–14076, Oct. 2024.
[17] B.-G. Choi and Y.-S. Kim, "New structure design of ferrite cores for wireless electric vehicle charging by machine learning," *IEEE Trans. Ind. Electron.*, vol. 68, no. 12, pp. 12162–12172, Dec. 2021.
[18] P. A. J. Lawton, F. J. Lin, and G. A. Covic, "Magnetic design considerations for high-power wireless charging systems," *IEEE Trans. Power Electron.*, vol. 37, no. 8, pp. 9972–9982, Aug. 2022.
[19] C. Chen, C. Q. Jiang, S. Ren, W. Guo, T. Ma, and Z. Luo, "Thermal enhancement of permeability-gradient nanocrystalline toroidal core with uniform magnetic flux density distribution," *IEEE Trans. Power Electron.*, vol. 40, no. 4, pp. 5661–5671, Apr. 2025.
[20] Y. Li, Z. Luo, Y. Li, J. Zhu, B. Zhang, and J. Zou, "Modeling of fe-based soft magnetic materials for multiphysical analysis of medium-frequency transformers," *IEEE Trans. Power Electron.*, vol. 39, no. 10, pp. 12249–12260, Oct. 2024.
[21] M. Budhia, G. A. Covic, and J. T. Boys, "Design and optimization of circular magnetic structures for lumped inductive power transfer systems," *IEEE Trans. Power Electron.*, vol. 26, no. 11, pp. 3096–3108, Nov. 2011.
[22] P. A. J. Lawton, F. J. Lin, and G. A. Covic, "Magnetic design considerations for high-power wireless charging systems," *IEEE Trans. Power Electron.*, vol. 37, no. 8, pp. 9972–9982, Aug. 2022.
[23] J. Smolka and A. J. Nowak, "Experimental validation of the coupled fluid flow, heat transfer and electromagnetic numerical model of the medium-power dry-type electrical transformer," *Int. J. Therm. Sci.*, vol. 47, pp. 1393–1410, Feb. 2008.
[24] G. R. Rodriguez, L. Garelli, and M. Storti, "Numerical and experimental thermo-fluid dynamic analysis of a power transformer working in ONAN mode," *Appl. Therm. Eng.*, vol. 112, pp. 1271–1280, Aug. 2016.
[25] G. Bertotti, "General properties of power losses in soft ferromagnetic materials," *IEEE Trans. Magn.*, vol. 24, no. 1, pp. 621–630, Jan. 1988.
[26] D. Kraus, G. A. Covic, H.-G. Herzog, P. A. J. Lawton, and F. J. Lin, "Design and assessment of an interoperable wireless power transfer system using an impedance-based method," *IEEE Trans. Power Electron.*, vol. 38, no. 2, pp. 2768–2781, Feb. 2023.
[27] Y. Wei, X. Zhang, Z. Chen, F. Xu, and C. K. Tse, "Ferrite core magnetothermal equilibrium design for wireless power transfer systems using a novel differential regulation coil," *IEEE Trans. Power Electron.*, vol. 40, no. 9, pp. 14084–14098, Sep. 2025.
[28] M. Hu and U. K. Madawala, "Magnetic structure design in IPT systems based on topology optimization," *IEEE Trans. Transp. Electrific.*, vol. 11, no. 2, pp. 5374–5386, Apr. 2025.

Xian Zhang received the M.E. and Ph.D. degrees in electrical engineering from the Hebei University of Technology, Tianjin, China, in 2009 and 2012, respectively.

He is currently a Professor with the Hebei University of Technology. He is the Director of the China Electrotechnical Society and the Secretary General of the National Specialized Committee on Wireless Power Transmission Technology. His research interests encompass intelligent high-power wireless power transmission technology, measurement of three-dimensional electromagnetic fields, and numerical calculations of modern engineering electromagnetic fields.

Jie Liu received the B.S. degree in electrical engineering and automation, in 2023, from the Hebei University of Technology, Tianjin, China, where he is currently working toward the M.E. degree in electrical engineering.

His research interests include engineering electromagnetism, wireless power transfer, and its industrial applications.

Runtian Dou was born in China, in 1994. He received the Ph.D. degree in electrical engineering from the Hebei University of Technology, Tianjin, China, in 2025.

He was a Visiting Ph.D. student with the Department of Electrical, Computer, and Software Engineering, The University of Auckland, from 2022 to 2023, working with Prof. A. P. Hu. His research interests include wireless power transfer technologies, high-frequency magnetic components, novel soft magnetic material, magnetic field modeling, and power electronics in electric vehicles.

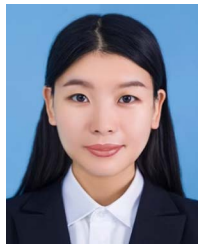

Liyuan Zhao was born in China, in 1992. She received the Ph.D. degree in electrical engineering from Tianjin University, Tianjin, China, in 2022.

She is currently a Lecturer with Hebei University of Technology, Tianjin, China. Her research interests include energy management and applications of artificial intelligence in power and energy systems.

Zhicheng Xu received the Ph.D. degree in engineering from Southeast University, Nanjing, China, in 2022.

He is currently an Associate Professor, Doctoral Supervisor, and Deputy Director of the Department of Smart Energy, the School of Electrical Engineering, Hebei University of Technology, Tianjin, China. He has presided over one National Natural Science Foundation of China project and one subproject of the National Key R&D Program of China. His main research interests include operation and maintenance management and control of electrochemical energy storage systems, and wireless intelligent sensors.

Jinghui Song received the B.S. degree in electrical engineering and automation, in 2023, from the Hebei University of Technology, Tianjin, China, where he is currently working toward the M.E. degree in electrical engineering.

His research interests include engineering electromagnetism, wireless power transfer, and its industrial applications.

Shenghu Liu received the B.S. degree in electrical engineering from Henan Polytechnic University, Jiaozuo, China, in 2023. He is currently working toward the M.E. degree in electrical engineering with the Hebei University of Technology, Tianjin, China.

His research interests include engineering electromagnetism, wireless power transfer, and its industrial applications.